Simulation of a rotor in forward flight to characterize helicopter wake signature and encounter severity

Guillaume Querinjean[1*], Victor Colognesi[1], Matthieu Duponcheel[1], Gilles Poncelet[1], Denis-Gabriel Caprace[1], Philippe Chatelain[1], Grégoire Winckelmans[1]

[1]Institute of Mechanics, Materials and Civil Engineering, UCLouvain, Louvain-la-Neuve, 1348, Belgium.

*Corresponding author(s). E-mail(s): guillaume.querinjean@uclouvain.be;
Contributing authors: victor.colognesi@uclouvain.be; matthieu.duponcheel@uclouvain.be; gilles.poncelet@uclouvain.be; denis-gabriel.caprace@uclouvain.be; philippe.chatelain@uclouvain.be; gregoire.winckelmans@uclouvain.be;

Abstract

The development of safe and efficient air traffic separation policies relies on the accurate quantification of the wake turbulence generated by aircraft and rotorcraft, and on the accurate understanding of the upset experienced by a follower aircraft or rotorcraft if encountering such wakes. To date, most research on wake turbulence has focused exclusively on fixed-wing aircraft. To address the existing gap in rotorcraft-specific studies, this paper first presents Large Eddy Simulations of the wake produced by a helicopter rotor in forward flight, performed using the Vortex Particle-Mesh method coupled with a multi-body solver. The effect of the airspeed is investigated, from a high value of 100 kt to a low value of 12.5 kt. For each case, the wake is characterized at equivalent dimensionless ages, and the wake-induced hazard produced on a follower fixed-wing reference aircraft is quantified using the rolling moment coefficient (RMC) metric. At low airspeeds, the wake departs from the rolled-up wake configuration typical of fixed-wing aircraft and rotorcraft flying at high airspeed, exhibiting increased vortex spacing and higher turbulence levels. The inverse proportionality between flight speed and vortex circulation is also shown to break down; the RMC value saturates, and it also rapidly decreases downstream. In a second scenario, the rotorcraft is considered as a follower flying through a wake. For three airspeeds of the follower rotorcraft (100 kt, 50 kt, and 25 kt), simulations of the rotor flying quasi-steadily through rolled-up wake vortices are performed, and the resulting aerodynamic loads are quantified. The wake-induced pitching moment, which is the dominant perturbation, is found to scale with the airspeed of the follower rotorcraft. A pitching moment severity metric is evaluated against the numerical simulation: while it provides a useful first-order estimate, it fails to capture the observed speed dependence.

Keywords: Rotorcraft, Wake turbulence, Wake encounter, Vortex Particle-Mesh method, Large Eddy Simulation

List of symbols

b	Aircraft wing span
b_0	Wake vortices spacing
D	Main rotor diameter
L	Lift force
$L_{x/y/z}$	Dimensions of the CFD domain
M_{Roll}	Rolling moment
M_{Ritch}	Pitching moment
M_{Yaw}	Yawing moment
r	Distance to a vortex center
r_c	Vortex core radius
t	Wake age
t^*	Dimensionless wake age
t_0	Wake vortex characteristic time
$\boldsymbol{u}$	Velocity field
u_θ	Vortex induced velocity
$\boldsymbol{u}_\omega$	Rotational velocity field
V_0	Wake vortex characteristic velocity
x	Streamwise coordinate
U_∞	Flight speed
y	Lateral coordinate
z	Vertical coordinate
β	Blade flap angle
$\Gamma(r)$	Vortex circulation distribution
Γ_0	Total vortex circulation
$\tilde{\Gamma}_0$	Half-plane circulation
ν	Air kinematic viscosity
θ	Blade pitch angle
θ_0	Collective pitch angle
θ_{1c}	Longitudinal cyclic pitch angle
θ_{1s}	Lateral cyclic pitch angle
$\theta_{1s,eq}$	Equivalent cyclic angle
$\theta^*_{1s,eq}$	Theoretical equivalent cyclic angle
ρ	Air density
$\boldsymbol{\omega}$	Vorticity field
ω_x	Axial vorticity component
Ω	Rotor angular velocity
$\lVert\cdot\rVert$	Vector norm
$\overline{\cdot}$	Time-averaging operator
AC	Fixed-wing aircraft
RC	Rotorcraft
RMC	Rolling moment coefficient
TAS	True Airspeed
VPM	Vortex Particle-Mesh
ILL	Immersed Lifting Line

1 Introduction

The projected growth of air traffic in the coming decades, coupled with increasing concerns over environmental and noise impacts, will stress future air traffic control systems in unprecedented ways. These pressures will create major operational and safety challenges, particularly for capacity-limited airports seeking to maximize runway throughput. In this context, optimizing safe air traffic separation policies becomes essential. Yet, most research on wake turbulence, which has led to widely adopted wake severity metrics, has focused exclusively on fixed-wing aircraft. Rotor-wing aircraft, such as helicopters, have largely been omitted, mainly due to the limited number of airports concerned with significant rotorcraft traffic. Unlike fixed-wing aircraft, which primarily operate along standardized runway-based trajectories, rotorcraft operate in a wider range of flight regimes and environments, including hover, low-speed transitions, and non-runway-based operations. While these differences modify the operational context of wake encounters, they do not eliminate the associated hazards, particularly in mixed fixed-wing/rotorcraft traffic and dense terminal airspace. To address this gap, this paper examines rotorcraft (here limited to conventional helicopters) in two roles: as a leader generating wake turbulence, and potentially posing a hazard to a follower aircraft; and as a follower encountering a wake. These two configurations define the distinct research questions explored here: (1) characterization of the wake turbulence produced by a rotorcraft, and also of the perturbation (rolling moment coefficient) on a follower aircraft; and (2) characterization of the perturbation (mainly in pitching moment) experienced by a follower rotorcraft flying through a wake.

1.1 Rotorcraft wake turbulence

Aircraft separation policies rely on a detailed understanding of the wake generated by aircraft in approach configuration. While the wakes of fixed-wing aircraft have been extensively investigated in previous studies [1, 2] and used in high-impacting wake severity metrics such as RECAT-EU [3], a substantial scientific gap remains regarding rotor-wing wake properties. Fatal accidents involving rotorcraft wakes have been reported [4, 5]. Although some guidance exists, such as the recommended three-rotor-diameter separation distance [6], it fails to cover the full range of rotorcraft flight configurations encountered in airport operations. During final approach, taxi, or departure, helicopter airspeeds can vary from their rated airspeed down to almost zero, causing more potent wake vortices at lower speeds. This wide airspeed range, combined with the intrinsic complexity of rotorcraft wakes, complicates the development of suitable severity metrics for wakes from rotorcraft.

Several experimental campaigns in the 20th century investigated rotorcraft wake properties and associated hazard, mainly by measuring the vortex-induced velocity field and the upset experienced by an aircraft crossing the wake. In the early 1960s, NASA flight tests [7] found a general similarity between fixed-wing rotor-wing wake effects (in forward flight) and recommended a one-minute separation. In the 1990s, a FAA study [8] using LIDAR wake measurements identified two flight-speed regimes. Above 40 kt, wake vortex circulation was proportional to rotorcraft weight and inversely proportional to airspeed; below 40 kt, this trend no longer held as the wake vortex structure began to break down. A DLR study [9] later highlighted the need for further investigation in the transition region between approach and hover, where vortex strength is expected to peak as airspeed approaches zero.

At low airspeeds, the wake's turbulent and skewed nature limits the usefulness of LIDAR-based measurements such as [8, 9], emphasizing the need for numerical simulations [10]. Yet numerical studies remain scarce. As noted in [10], most works [11–14] have focused on the near-rotor wake due to its influence on rotor performance, noise, and vibration. Far-wake analysis remains challenging for conventional CFD methods (e.g., finite volume solvers), which suffer excessive numerical diffusion, underscoring the necessity of high-fidelity and vorticity-based numerical approaches [14]. In [15], three wake modeling methods were compared and applied to simulate a wake encounter event, though without yielding quantitative wake characterization. In [10], an attempt was made to extend the RECAT-EU methodology to rotor-wing aircraft by classifying helicopters based on weight and rotor diameter. However, due to the use of a simplified wake model, that study did not address low advance ratio configurations, pointing to the need for high-fidelity simulations at low airspeeds.

To bridge the gap in rotorcraft-specific far-wake studies (particularly at low airspeeds), this paper provides an in-depth characterization of a helicopter wake in forward flight and covering a wide airspeed range: 100, 50, 25 and 12.5 kt. In addition to a qualitative wake description, a systematic quantitative analysis of key wake properties (vortex circulation and induced velocity profiles) is conducted. The associated potential hazard on a follower fixed-wing aircraft is assessed using the rolling moment coefficient (RMC) metric, also employed in RECAT-EU. To this end, Large Eddy Simulations (LES) are performed, using the hybrid Vortex Particle-Mesh (VPM) method with Immersed Lifting Lines (ILL) to represent the blades. Thanks to its hybrid Lagrangian-Eulerian formulation, this approach combines numerical performance with minimal numerical diffusion and dispersion errors, enabling wake capture over tens of rotor diameters downstream [16, 17]. The method was also validated against experimental data in [18].

1.2 Rotorcraft wake encounter

An accurate understanding of rotorcraft response during wake encounters is essential for developing future separation policies involving follower rotorcraft. Since the late 1970s, several studies have addressed this issue. Early experiments [19–21] assessed helicopters encountering the wake from fixed-wing aircraft and concluded that such events posed limited hazard. Concurrently, numerical investigations using simplified representations of the vortex-induced and rotor-induced velocity fields [22] challenged this view, revealing the potential dangerous character of encounter events. Subsequent works [23, 24] improved the numerical modeling of vortex effects on rotor aerodynamics, showing that wake encounters mostly induce a pitching moment perturbation on the rotorcraft. Later advancements in aerodynamics fidelity [25, 26] further refined these models; yet methodological inconsistencies across studies prevented general conclusions about rotorcraft wake encounter safety [27].

In the 2000s, numerical approaches evolved to include quasi-static, fully dynamic, and pilot-in-the-loop simulations. Using FLIGHTLAB, [28] simulated the full multibody dynamics of a helicopter experiencing a single-vortex wake encounter, quantifying its pitch and vertical responses under the "frozen vortex" assumption. In the latter, the rotor and vortex wakes are superimposed linearly, which effectively suppresses the influence of the rotor wake on the vortex. Using the same assumption, [29] found the pitch upset to depend on the follower airspeed in a non-monotonic fashion. Later studies [27, 30] employed the Vorticity Transport Model (VTM), which captures the blade-wake and wake-wake interactions, to compare several numerical modeling techniques, with the primary objective of challenging the frozen vortex assumption. Their results indicated that this simplification is valid only at high airspeeds. At lower airspeeds, the frozen vortex method fails to capture the dynamic character of long-time encounters and over-predicts the encounter severity. As most near-airfield rotorcraft operations occur at low airspeeds, these studies called for higher-fidelity simulations. Further dynamical simulations using the FLIGHTLAB environment were conducted in [31, 32], again using the frozen vortex hypothesis. In [31], a simplified encounter severity metric is proposed, considering an analogy between the transverse distribution of vortex-induced velocity and a linear velocity distribution across the rotor disc. However, their study also underlined the need for further research to ascertain the validity of the superposition principle.

Despite these efforts, the current state of the art still lacks high-fidelity simulations of rotorcraft wake encounters at low airspeeds that do not rely on the frozen-vortex hypothesis, which is known to break down in this regime. The present paper addresses this gap by performing fully coupled simulations of a helicopter flying through a rolled-up wake, including at low airspeeds, thereby accounting for the two-way interaction between the rotor and the wake. By providing a more realistic characterization of rotorcraft wake encounters at low airspeeds, this work directly supports the development of physics-based wake-separation criteria for rotorcraft in mixed traffic. The simulations are again performed in LES using the VPM-ILL framework. One should note that since the wake vortex core is significantly larger than the blade chord, the ILL approach can capture the wake-rotor interactions and hence produce realistic wake vortex deformations. Encounters are simulated with the rotorcraft flying at 100, 50 and 25 kt, and crossing a fully developed two-vortex system at low lateral speed, thus corresponding to a long-time encounter. This setup focuses exclusively on the aerodynamic interaction between the rotor and the wake vortices and on the resulting forces and moments, representing worst-case loading conditions. The rotorcraft kinematics (i.e., the 6 degrees of freedom of the helicopter and those of the blade joints) are prescribed; the blade flapping being of course left free and dynamically computed. Finally, the pitching moment severity metric proposed in [31] is then also evaluated against the VPM-ILL simulation results at the various airspeeds.

2 Method

The present work builds upon Large Eddy Simulations of a four-bladed rotor based on available data of the Airbus Helicopter H135 main rotor, performed using a numerical method coupling the multi-body integrator `ROBOTRAN` with a massively parallel Vortex Particle-Mesh (VPM) solver. The former is responsible for the rigid blade dynamics and rotor control inputs, and the latter for the bulk flow simulation.

2.1 Flow solver

The flow solver [33] relies on a hybrid Lagrangian-Eulerian formulation of the incompressible ($\nabla \cdot \boldsymbol{u} = 0$) Navier-Stokes equations in their vorticity-velocity formulation ($\boldsymbol{\omega} - \boldsymbol{u}$):

$$\frac{D\boldsymbol{\omega}}{Dt} = (\nabla \boldsymbol{u}) \cdot \boldsymbol{\omega} + \nu \nabla^2 \boldsymbol{\omega} + \nabla \cdot \left(\nu_{sgs} \left(\nabla \boldsymbol{\omega}^s - (\nabla \boldsymbol{\omega}^s)^T \right) \right) \tag{1}$$

where $\frac{D}{Dt} \triangleq \frac{\partial}{\partial t} + \boldsymbol{u} \cdot \nabla$ denotes the material derivative, ν_{sgs} the eddy viscosity provided by the sub-grid scale model required for Large Eddy Simulations, and $\boldsymbol{\omega}^s$ a filtered version of the vorticity field. The incompressible velocity field is decomposed as

$$\boldsymbol{u} = \boldsymbol{U}_\infty + \boldsymbol{u}_{\boldsymbol{\omega}} \tag{2}$$

where $\boldsymbol{U}_\infty$ is the free stream velocity (i.e., the flight speed) and $\boldsymbol{u}_{\boldsymbol{\omega}}$ is retrieved from the vorticity field through the resolution of a Poisson equation:

$$\nabla^2 \boldsymbol{u}_{\boldsymbol{\omega}} = -\nabla \times \boldsymbol{\omega} \; . \tag{3}$$

The advection term of the Navier-Stokes equations, which corresponds to the left-hand side of Eq. (1), is handled using Lagrangian vorticity-carrying particles, each characterized by a position $\boldsymbol{x}_p$ and a strength $\boldsymbol{\alpha}_p = \int_{V_p} \boldsymbol{\omega} \; d\boldsymbol{x}$, where V_p corresponds to the material volume associated to the particle. This Lagrangian treatment of the flow allows to write Eq. (1) as two sets of ODE's for the particles:

$$\frac{d\boldsymbol{x}_p}{dt} = \boldsymbol{u}\left(\boldsymbol{x}_p\right) \; , \tag{4}$$

$$\frac{d\boldsymbol{\alpha}_p}{dt} = \int_{V_p} \left[(\nabla \boldsymbol{u}) \cdot \boldsymbol{\omega} + \nu \nabla^2 \boldsymbol{\omega} + \nabla \cdot \left(\nu_{sgs} \left(\nabla \boldsymbol{\omega}^s - (\nabla \boldsymbol{\omega}^s)^T \right) \right) \right] \; d\boldsymbol{V}_p \; . \tag{5}$$

Both ODE's are integrated in time using a third-order Runge-Kutta scheme.

The right-hand side of Eq. (5), which comprises the stretching, diffusion and LES terms, is discretized using fourth-order finite differences on an underlying Cartesian mesh, thus conferring a Eulerian character to the solver.

The Poisson equation Eq. (3) must be solved at each timestep to retrieve the velocity field. Its numerical resolution also exploits the background Cartesian mesh, as it is solved in Fourier space using the PPM library [34]. This allows the enforcement of unbounded and inlet/outlet boundary conditions.

In Large Eddy Simulations, only a fraction of the turbulence scales are resolved. The unresolved fine scales must taken into account through an added sub-grid scale (SGS) model. To this end, a simplified version of the regularized variational multiscale model (RVM) is used. In this model, the effective eddy viscosity ν_{sgs} only operates on the filtered LES vorticity field, $\boldsymbol{\omega}^s$. The effective eddy viscosity is obtained as $\nu_{sgs} = C_R h^2 \left(2 S_{ij} S_{ij}\right)^{1/2}$, with C_R a constant coefficient, h the grid cell size, and S_{ij} the strain rate tensor. The filtered vorticity field is obtained by applying several times an explicit discrete filter. Additional details can be found in [35].

The hybrid particle-mesh discretization of the flow requires mesh-to-particles and particles-to-mesh interpolations, which are carried out using high-order kernel schemes. To alleviate the loss of accuracy due to particle clustering and depletion, a periodic remeshing of the particles is performed by redistributing the vorticity they carry onto the underlying mesh. As the method does not preserve the solenoidal character of the vorticity field ($\nabla \cdot \boldsymbol{\omega} = 0$), the vorticity field is also periodically reprojected onto a divergence-free space by solving a Poisson equation (additional details can be found in [36]).

The Vortex Particle-Mesh method exploits the non-dispersive properties of Lagrangian methods, enabling very accurate capture of turbulent wakes over extreme distances. It also permits the use of larger time steps by partially waiving the classical Courant–Friedrichs–Lewy condition associated with Eulerian methods.

The flow is not fully resolved around the rotor blades, i.e., the fine-scale boundary layer phenomena are not captured. Instead, the coarse-scale aerodynamics are modeled through an Immersed Lifting Line (ILL) method [37, 38], which discretizes the blades into finite segments, where aerodynamic forces are obtained from airfoils polars. More specifically, a third generation Leishman-Beddoes Dynamics Stall model [39] uses the instantaneous flow velocity and blade angle of attack to compute the lift and drag exerted on each local 2D airfoil. Then, the circulation around the airfoil is recovered from

$$\boldsymbol{l} = \rho\, \boldsymbol{V}_{\mathrm{rel}} \times \boldsymbol{\Gamma} \tag{6}$$

with $\boldsymbol{l}$ the lift per unit span of the segment, $\boldsymbol{V}_{\mathrm{rel}}$ the relative flow velocity and $\boldsymbol{\Gamma}$ the circulation. This circulation on a given blade segment is represented by an equivalent bound vorticity, which is then transferred to the VPM method through the release of particles carrying the shed vorticity in the bulk flow. The latter is deduced from the temporal and spanwise variations of the bound vorticity.

In order to better match realistic atmospheric conditions, the flow solver allows the injection of turbulence at the inflow of the numerical domain, which is pre-generated using the Mann algorithm [40, 41].

2.2 Multi-body solver and rotor configuration

The rigid-body mechanics of the rotor are captured through a weak coupling between the flow solver and the multi-body integrator `ROBOTRAN` [42], which efficiently solves the direct dynamics of the multi-body system formed by the rotor hub and blades. In this coupling, `ROBOTRAN` uses a separate temporal integrator to advance in time the state of the multi-body system, based on the aerodynamic forces computed by the flow solver and on the rotor control inputs. After each iteration, the new positions of the lifting bodies are communicated back to the flow solver.

In the present work, a simple rotor model is used. It consists of a rotor shaft rotating at a prescribed angular velocity Ω, connected to four rigid blades through hinges allowing two degrees of freedom per blade, namely the flap angle β and the pitch angle θ. The position and orientation of the rotor are prescribed. The blade flapping motion results from the inertial and aerodynamic efforts exerted on the blades. The blade pitch is prescribed to cancel the rolling and pitching moments at the rotor hub and to achieve the desired thrust target. This is done using the usual collective-cyclic decomposition:

$$\theta = \theta_0 + \theta_{1s} \sin \Psi + \theta_{1c} \cos \Psi \tag{7}$$

where θ_0 is the collective, θ_{1s} the lateral cyclic, θ_{1c} the longitudinal cyclic and Ψ the blade azimuthal angle (equal to zero when the blade is pointing downstream). In this work, the control input values θ_0, θ_{1s}, and θ_{1c} used in the production runs are obtained in preliminary trim simulations using a closed-loop PI controller.

The mass of the helicopter is taken as 3000 kg. Rotor parameters are provided by [43]. The main rotor diameter D is 10.2 m and its angular velocity is fixed to 395 RPM. Thus, the considered advance ratios are μ = 0.096, 0.192, 0.383, and 0.766, respectively at 12.5, 25, 50, and 100 kt. The airfoil profile used in the ILL approach is a NACA0015. The hub diameter is 0.35 m. The chord length is 0.29 m and is linearly tapered at the root and tip. The blade twist is 10°.

3 Rotorcraft wake characterization

This section reports the characterization of the wake shed by a rotorcraft flying at four different airspeeds: 100, 50, 25, and 12.5 kt, which are representative of various approach, landing, and taxiing flight configurations. The main objective of the study is the characterization and comparison of the wake signature at those flight speeds. The wake properties are also compared to those of the wake shed by an aircraft of similar mass flying at a typical approach speed of 100 kt.

A second objective is the assessment of the robustness of the simplified wake encounter severity metric for a follower aircraft encountering those wakes, namely, the rolling moment coefficient (RMC) metric, widely used in RECAT-EU [3].

3.1 Numerical setup

The flow solver uses a uniform mesh resolution. For each case considered in this section, the spatial resolution is set to 96 grid points per rotor diameter (i.e., a Cartesian cell size of 10.625 cm), which represents a compromise between accuracy and time-to-solution. The computational domain is a rectangular box, with dimensions that depend on the extent of the support of the vorticity field and, therefore, on the flight speed: at high TAS, the wake is more compact but must be simulated farther downstream. This is because the evaluation of the wake properties must be performed at a similar dimensionless age t^* for each TAS. The dimensionless age of the wake at a given downstream position x is

$$t^* = \frac{t}{t_0} = \frac{x}{U_\infty\, t_0} \tag{8}$$

where

$$t_0 = \frac{b_0}{V_0} \quad \text{and} \quad V_0 = \frac{\Gamma_0}{2\pi\, b_0} \tag{9}$$

with b_0 the distance between the centers of the two rolled-up wake vortices and $\pm\Gamma_0$ the total circulation of each vortex (one being positive, the other one being negative). Therefore

$$t^* = \frac{\Gamma_0\, x}{U_\infty\, 2\pi\, b_0^2} = \frac{L\, x}{\rho\, U_\infty^2\, 2\pi\, b_0^3}\ . \tag{10}$$

At constant lift $L = \rho\, U_\infty\, \Gamma_0\, b_0$ and assuming b_0 remains essentially constant, Γ_0 is inversely proportional to the TAS. Therefore, the downstream distance at which the wake reaches the same dimensionless age is proportional to the square of the TAS: when the TAS is halved, the distance at which the wake properties should be evaluated is divided by four. While this argument does not strictly hold for rotorcraft at low airspeeds–since the lift equation becomes only approximate and b_0 varies (as discussed later)–it still provides a reasonable approximate scaling.

In all cases, the computational domain extends $4D$ upstream of the rotor center. The domain dimensions for the different airspeeds considered are summarized in Table 1. The x axis is aligned with the free stream velocity (positive direction pointing downstream), and the z axis points upwards. The approximate total number of grid points for each simulation is 113×10^6, 71×10^6, 170×10^6, and 382×10^6, respectively for 100, 50, 25, and 12.5 kt.

For each case, the simulation is first run for one convective time $t_c = L_x/U_\infty$ to allow the wake to fully develop. At 100, 50 and 25 kt, wake statistics are computed over an additional two convective times; at 12.5 kt, they are computed over one additional convective time.

Turbulence is injected at the inflow to simulate a weakly turbulent atmosphere, with an eddy dissipation rate of $\epsilon = 1.59 \times 10^{-5}\,\mathrm{m}^2\,\mathrm{s}^{-3}$.

Table 1 Dimensions of the computational domain

$\mathbf{U}_\infty$	[kt]	**100**	**50**	**25**	**12.5**
$\boldsymbol{L_x/D}$	[−]	32	20	12	12
$\boldsymbol{L_y/D}$	[−]	2	2	4	6
$\boldsymbol{L_z/D}$	[−]	2	2	4	6

3.2 Qualitative wake characteristics

Figures 1, 2, 3, and 4 show 3D volume renderings of the instantaneous vorticity magnitude, $\|\boldsymbol{\omega}\|$, for the wake produced by a rotorcraft flying at 100 kt, 50 kt, 25 kt, and 12.5 kt.

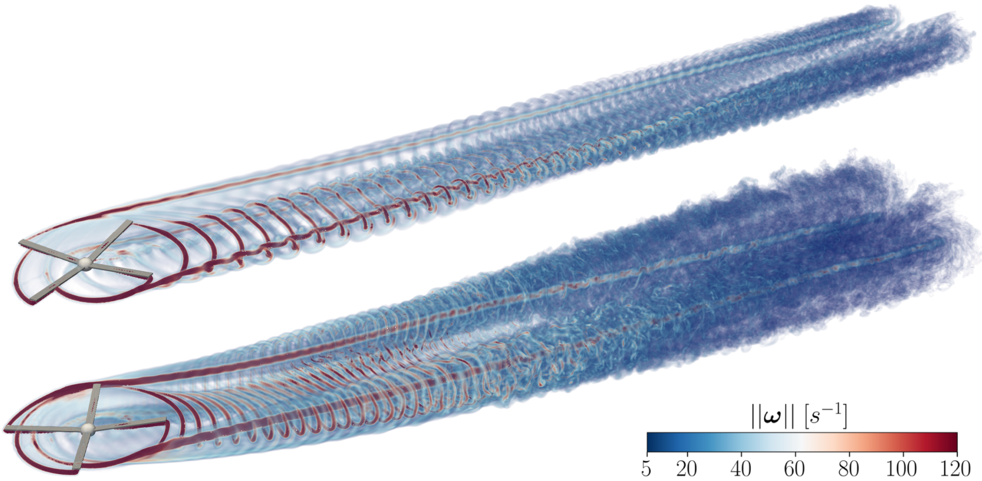

Fig. 1 Volume rendering of $\|\boldsymbol{\omega}\|$ showing the wake at 100 kt (top) and 50 kt (bottom)

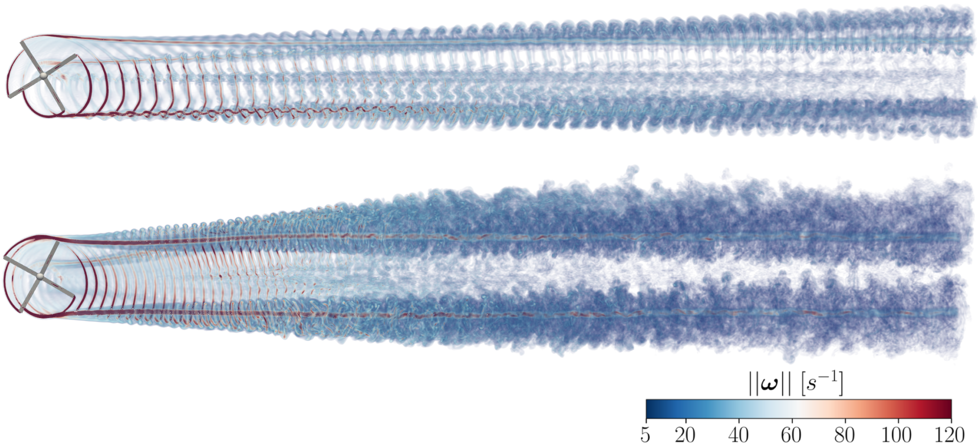

Fig. 2 Volume rendering of $\|\boldsymbol{\omega}\|$ showing the wake at 100 kt (top) and 50 kt (bottom)

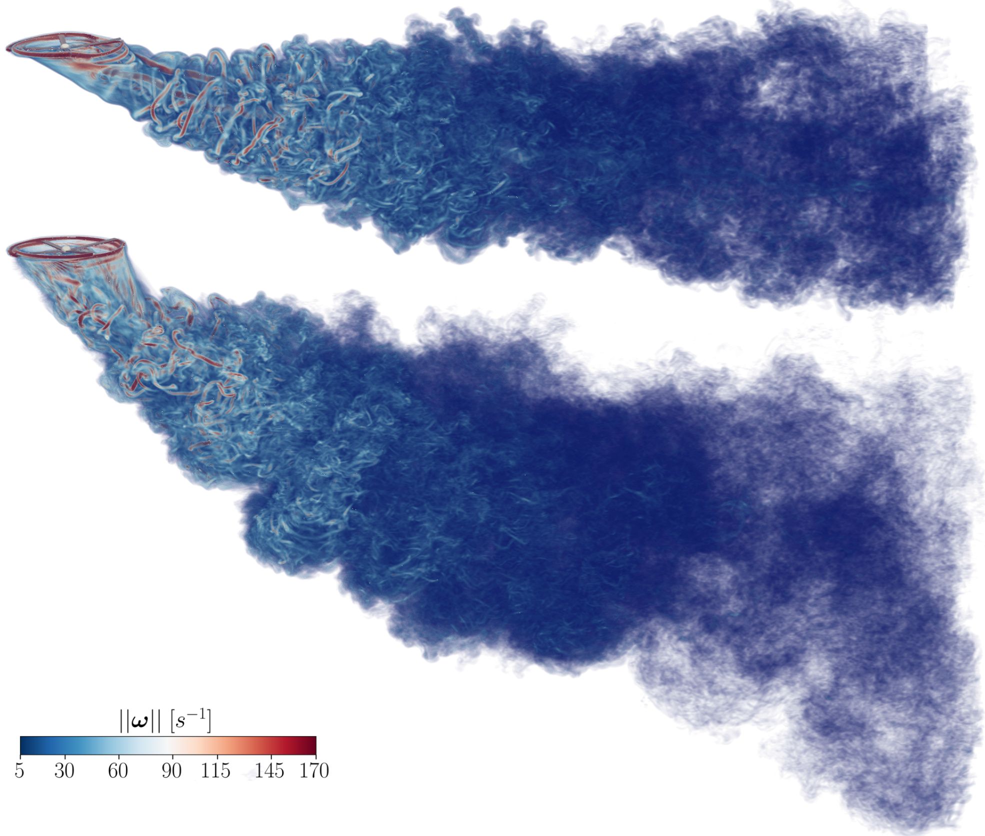

Fig. 3 Volume rendering of $\|\boldsymbol{\omega}\|$ showing the wake at 25 kt (top) and 12.5 kt (bottom)

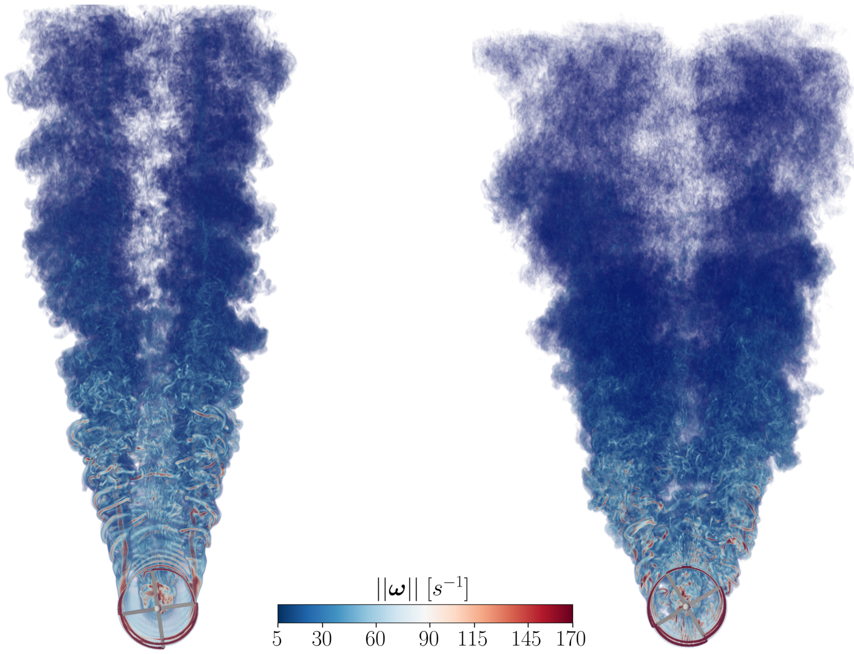

Fig. 4 Volume rendering of $\|\omega\|$ showing the wake at 25 kt (left) and 12.5 kt (right)

At high and moderate airspeeds (100 and 50 kt), the wake rolls up in a pair of counter-rotating vortices, which are clearly visible in Figures 1 and 2. The wake is very similar to that of a fixed-wing aircraft, with well distinguishable vortices. At low airspeed (25 kt), the wake rolls up to form a coherent two-vortex system, that is still visible in Figures 3-4 despite the greater complexity of the wake compared to the cases at higher TAS. At the very low speed of 12.5 kt (Figures 3-4), the wake resembles more a deformed turbulent jet. The wake vortices, although still measurable when investigating the time-averaged flow, are no longer visible in an instantaneous flow field: they are overwhelmed by the complex turbulent structures.

In the following investigations, the reported statistics and wake properties are measured in planes normal to the free stream velocity. In Eq. (10), it is shown that the distance downstream (evaluated in the x direction, and relative to the rotor center) where the wake properties must be evaluated is essentially proportional to the TAS squared. The wake properties are measured at a distance of $24D$ at 100 kt and $6D$ at 50 kt. At 25 kt, the distance should be $1.5D$, and at 12.5 kt, it should be $0.375D$, following the approximate scaling of Eq. (10). However, as shown in Figure 5 (representing the circulation distribution, $\Gamma(r)$, around the center of the wake vortices, taken as the mean of the distributions around the port and starboard vortices), the wake cannot properly roll up over such short distances. To have a rolled-up wake (i.e., one without an overshoot in $\Gamma(r)$), the evaluation distance is set to $x = 3D$ at 25 kt, and to $x = 1.5D$ at 12.5 kt.

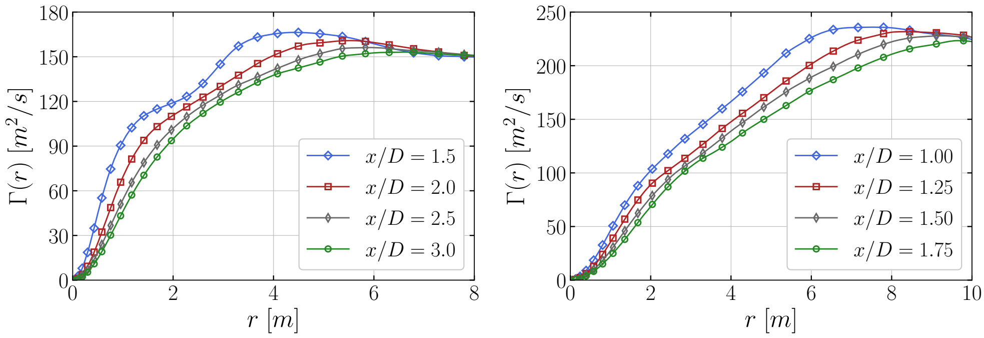

(a) $U_\infty = 25$ kt (b) $U_\infty = 12.5$ kt

Fig. 5 Wake rollup at $U_\infty = 25$ kt and $U_\infty = 12.5$ kt: distribution of circulation $\Gamma(r)$ at various downstream locations

When assessing the wake signature, it is useful to compute the time-averaged field of axial vorticity at a given downstream location x, $\overline{\omega_x}(x)$, from which one can retrieve meaningful mean wake characteristics such as the position of the vortices, their circulation and induced velocity distribution, and the core radius. Figure 6 shows slices of normalized mean axial vorticity field $\dfrac{\overline{\omega}_x D}{U_\infty}$ at 100, 50, 25, and 12.5 kt.

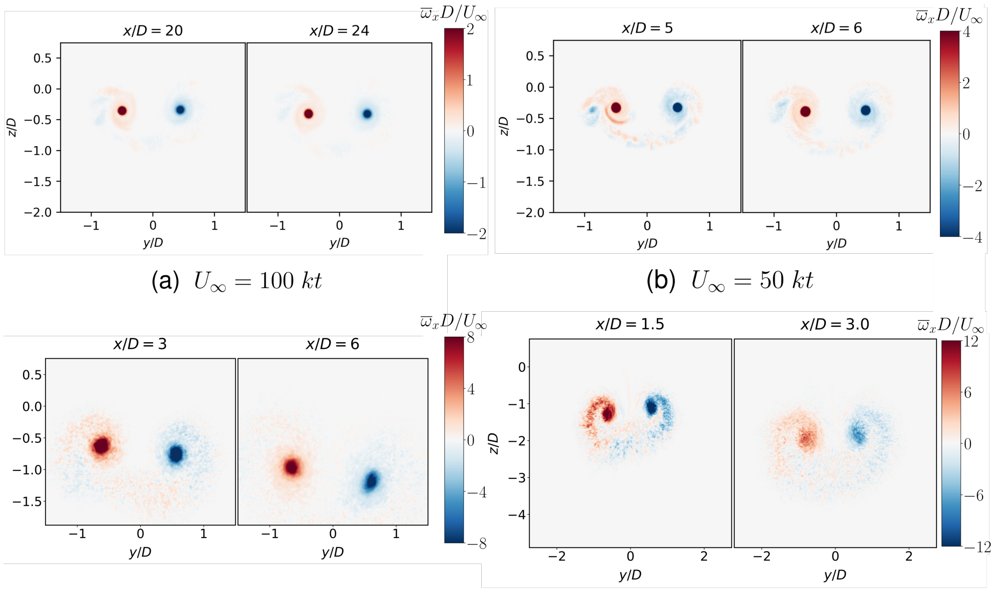

(a) $U_\infty = 100\ kt$ (b) $U_\infty = 50\ kt$

(c) $U_\infty = 25\ kt$ (d) $U_\infty = 12.5\ kt$

Fig. 6 Normalized mean axial vorticity at 100, 50, 25, and 12.5 kt

At 100 kt and 50 kt, the vortex cores are clearly visible in the time-averaged field, up to far downstream. The wake is port-starboard symmetric. At 25 kt, the vortex cores are more spread out and port-starboard asymmetric. At 12.5 kt, the two-vortex system appears (as a reminder, it is not visible in the instantaneous fields), but it is much more spread out and rapidly diffuses downstream.

3.3 Quantitative wake characterization

A quantitative comparison of the wake properties at the four airspeeds of interest is shown in Table 2. They are also compared to those of a fixed-wing aircraft flying at 100 kt. The aircraft is based on public data for the Daher-Socata TBM 900[1] (with a flap setting typical of a landing configuration), which has a span and mass similar to those of the rotorcraft (span $b = 12$ m and mass of 3000 kg), and is simulated using the same numerical setup as that used for the simulation of the rotorcraft flying at 100 kt. The position of the wake vortex cores is determined by optimizing the center position of a 2-D Gaussian kernel relatively to the time-averaged streamwise vorticity field. At a given streamwise location x, the circulation profile as a function of the distance to the vortex center, r, is then obtained by surface integration around the vortex core:

$$\Gamma(r) = \int_0^{2\pi} \int_0^{r} \overline{\omega}_x(x,\rho,\theta)\; d\rho\; d\theta \tag{11}$$

The vortex induced velocity is then obtained as $u_\theta(r) = \Gamma(r)/(2\pi r)$. The following quantities are measured:

- Γ_0, the maximum value of the measured circulation distribution $\Gamma(r)$ of the wake vortices,
- b_0, the measured distance between the two wake vortex cores,
- r_c, the effective core radius (defined as the radius of maximum vortex induced velocity),
- $\tilde{\Gamma}_0 = \int_{\text{half-plane}} \overline{\omega}_x\, dS$, the half-plane circulation,
- $\tilde{b}_0 = \dfrac{I}{\tilde{\Gamma}_0}$ where $I = \int y\, \overline{\omega}_x\, dS$ is the impulse.

When it is fully rolled-up, the wake shed by a wing consists of a pair of counter-rotating vortices of total circulation $\pm\Gamma_0$ and spacing b_0 between the vortex centers. The lift can then simply be expressed as a function of the flight speed and vortex properties:

$$L = \rho\, U_\infty\, \Gamma_0\, b_0\ . \tag{12}$$

In general, and as reported in [44], the lift produced by a lifting body, such as a wing or rotor, can be expressed as

$$L = \rho \left(U_\infty \int_S y\, \overline{\omega}_x\; dS - \int_S \left(\overline{u}_x - U_\infty\right) \overline{u}_z\; dS \right) \tag{13}$$

[1] Taken in the TBM 900 pilot's information manual, Daher-Socata, 2017

Table 2 Measured wake properties

Type		AC	RC	RC	RC	RC
$\mathbf{U_\infty}$	[kt]	**100**	**100**	**50**	**25**	**12.5**
$\boldsymbol{x}$	[m]	$24b$	$24D$	$6D$	$3D$	$1.5D$
$\boldsymbol{\Gamma_0}$	$[\mathrm{m^2\,s^{-1}}]$	52.3	52.2	101	153	228
$\boldsymbol{b_0}$	[m]	8.89	9.74	9.87	12.20	12.52
$\boldsymbol{r_c}$	[m]	0.63	0.69	0.66	1.41	2.19
$\boldsymbol{\tilde{\Gamma}_0}$	$[\mathrm{m^2\,s^{-1}}]$	52.5	50.5	97.1	148	223
$\boldsymbol{\tilde{b}_0}$	[m]	9.09	9.30	9.72	12.63	16.05

where S is a plane normal to the free stream velocity and enclosing the support of ω_x. If the axial velocity difference $\overline{u}_x - U_\infty$ (induced by the wake and also due to the parasitic drag) is negligible, Eq. (13) reduces to

$$L = \rho\, U_\infty \int_S y\overline{\omega}_x \; dS = \rho\, U_\infty\, \tilde{\Gamma}_0\, \tilde{b}_0 \; . \tag{14}$$

When the wake consists of almost axisymmetric and compact vortices with a total circulation Γ_0 easily measurable, this equation reduces to Eq. (12).

At high (100 kt) and moderate (50 kt) airspeeds, the rotorcraft wake rolls up into a pair of compact, counter-rotating vortices, closely resembling those shed by a fixed-wing aircraft. As shown in Table 2, the wake characteristics of the aircraft and the rotorcraft flying at 100 kt are very similar, except for a slightly greater vortex spacing for the latter. At these TAS, b_0 does not vary significantly with U_∞, and Γ_0 provides a good estimate of the total half-plane circulation. Thus, the general lift Eq. (13) is well approximated by Eq. (12). In cases where b_0 remains approximately constant, the circulation Γ_0 is therefore essentially inversely proportional to TAS:

$$\Gamma_0 \propto \frac{1}{U_\infty}. \tag{15}$$

At low TAS (25 kt), the two-vortex system becomes more diffused, with a notable increase in core radius, though it remains relatively compact and axisymmetric. The vortex circulation can still be measured reliably. A notable finding is the significant increase in vortex spacing b_0, which now exceeds the rotor diameter D, with a ratio b_0/D of approximately 1.2. This comes as a somewhat surprising result. For fixed-wing aircraft, the vortex spacing is always smaller than the wingspan b (i.e., $b_0/b < 1$). However, this does not always hold for rotorcraft; it is true at high and moderate airspeeds, but not at low airspeeds. Since the b_0/D ratio at 25 kt differs from that at 50 and 100 kt, a consequence of Eq. (12) is that Γ_0 is no longer inversely proportional to U_∞; specifically, it does not double when U_∞ is halved.

At very low TAS (12.5 kt), the mean wake deviates significantly from a simple two-vortex system: the mean axial vorticity field is no longer axisymmetric about the vortex center, and its support is much less compact (see Figure 6). Although Eq. (14) remains valid, the vortex center is not clearly defined; even when measured approximately, it does not coincide with the centroid of the half-plane vorticity field (i.e., the measured b_0 differs significantly from $\tilde{b}_0$). Since the vorticity field is no longer axisymmetric about the measured vortex center, the notion of a circulation distribution depending solely on the radial distance r from the center becomes ill-defined, making the determination of a representative Γ_0 less straightforward.

It must be emphasized that Eq. (14) holds in all cases. When a two-vortex system is well-defined (i.e., with a clearly identifiable center and an essentially axisymmetric vorticity field around that center), the measured b_0 value closely approximates $\tilde{b}_0$, and the measured Γ_0 is similarly close to $\tilde{\Gamma}_0$; thus, Eq. (12) is also valid in such cases.

3.4 Distribution of circulation and induced velocity

Figure 7 (a) shows the radial distribution of dimensionless circulation $\Gamma(r)/\Gamma^*$ (where Γ^* is the circulation evaluated at $r = 0.7\, b_0$) for all cases studied, including the aircraft flying at 100 kt.

The wakes of the aircraft and the rotorcraft at 100 kt exhibit similar circulation distributions, although the aircraft presents a monotonous increase of $\Gamma(r)$, while the rotorcraft shows a slight overshoot. This suggests that the wake is not yet fully rolled up. It may require an additional 10–15D to reach a monotonous circulation distribution.

The distribution at 50 kt is very close to that at 100 kt for $r/b_0 \geq 0.2$, showing the same overshoot and likewise indicating an incomplete roll-up. Interestingly, it also closely matches that of the aircraft at 100 kt for $r/b_0 \leq 0.2$.

At 25 kt, the circulation distribution still resembles that observed at higher TAS, but with an effective core twice as wide. This similarity disappears at 12.5 kt, where the shape of the distribution is very different.

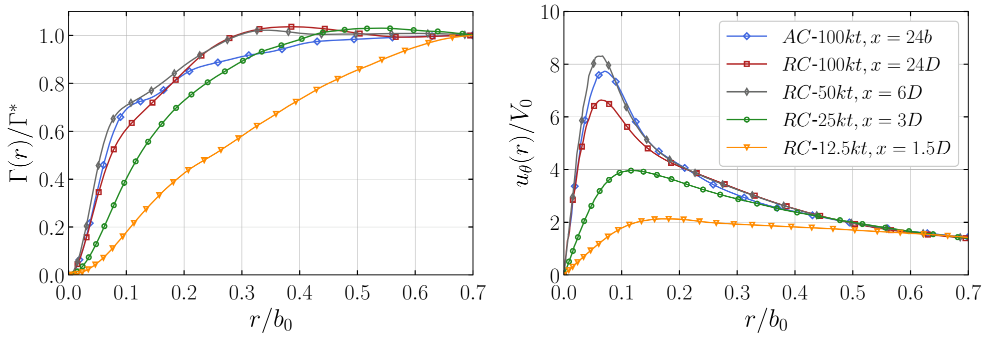

(a) Dimensionless circulation (b) Dimensionless induced velocity

Fig. 7 Radial distribution of circulation and induced velocity

The radial distribution of the dimensionless induced velocity $u_\theta(r)/V_0 = (\Gamma(r)/(2\pi\, r)/V_0)$ is shown in Figure 7 (b). The profiles for the aircraft and for the rotorcraft at 100 and 50 kt are relatively similar, due to their comparable core radius ratios, $r_c/b_0 \simeq 0.07$. At 25 kt, $r_c/b_0 \simeq 0.12$, leading to a noticeably lower maximum dimensionless induced velocity. At 12.5 kt, where $r_c/b_0 \simeq 0.18$, the maximum dimensionless induced velocity is further reduced.

3.5 RMC metric

The simplified wake severity metric used in RECAT-EU [3] estimates the normalized rolling moment imparted to a follower aircraft, assuming an encounter centered on a single wake vortex while neglecting the influence of the other. The rolling moment coefficient[2] (RMC) is estimated as:

$$RMC = \frac{M_{Roll}}{\frac{1}{2}\rho U_{\infty,f}^2\, S\, b} \simeq \frac{AR}{(AR+4)} \int_0^1 \frac{c(\eta)}{\bar{c}} \frac{\Gamma(\eta)}{U_{\infty,f}\, b}\, d\eta \tag{16}$$

where

- $U_{\infty,f}$ is the TAS of the follower aircraft,
- b is the span of the wing,
- S is the area of the wing,
- $\bar{c} = S/b$ is the mean chord of the wing,
- $AR = b/\bar{c}$ is the Aspect Ratio of the wing,
- $\eta = y/(b/2)$,
- $c(\eta)$ is the chord distribution of the wing.

The RMC metric is thus based on the measured circulation distribution around the wake vortex.

[2] As developed by UCLouvain and WaPT: G. Winckelmans and I. De Visscher. Complement note on metrics for the rolling moment coefficient and the equivalent roll rate due to encounter of an aircraft with a wake vortex. Technical report, UCLouvain, 2013.

In this study, the follower aircraft is the same as the leader aircraft used for the comparison of the wake properties, i.e., the Daher-Socata TBM 900 with $U_{\infty,f} = 100\ kt$. The values of RMC obtained for an encounter with the various wakes at a distance x_{enc} from the rotor/wing center are reported in Table 3.

Table 3 RMC values for a follower fixed-wing aircraft flying at $U_{\infty,f} = 100\ kt$

Generator		**AC**	**RC**	**RC**	**RC**	**RC**
$\mathbf{U}_\infty$	[kt]	**100**	**100**	**50**	**25**	**12.5**
$\boldsymbol{x}_{\text{enc}}$	[m]	$24b$	$24D$	$6D$	$3D$	$1.5D$
RMC	[−]	0.046	0.045	0.089	0.107	0.104

The RMC resulting from a centered encounter with a single vortex generated by the aircraft and the rotorcraft flying at 100 kt is nearly identical, reflecting the similarity of their induced velocity profiles. For the case of the rotorcraft flying at 50 kt, since r_c/b_0 is similar to that at 100 kt and the generator TAS is halved, the RMC doubles. In contrast, for the rotorcraft at 25 kt, the RMC increases by only about 20 %. At 12.5 kt, the RMC does not increase further.

It should be noted that, at low and very low TAS, the RMC becomes strongly dependent on the streamwise position at which it is measured, as illustrated in Figure 8. This is attributed to the rapid "aging process" of the wake vortices, which becomes significant when the wake is very turbulent and the effective core radius increases fast. Through this mechanism, the vortices interact significantly with each other through the mid-plane, causing a decrease in the circulation of each vortex. For the wake generated at 25 kt, the RMC decreases by 15 % between $x = 3D$ and $x = 6D$; for the 12.5 kt wake, the RMC drops by 48 % between $x = 1.5D$ and $x = 6D$.

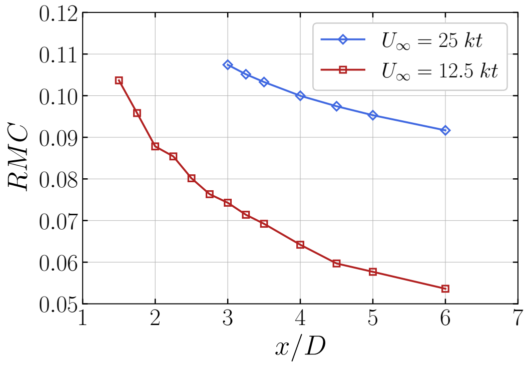

Fig. 8 Variation of the RMC with the normalized streamwise distance x/D for the wakes of rotorcraft at 25 kt and 12.5 kt

4 Rotorcraft flying through a wake

This section summarizes the results regarding the numerical simulations of a rotorcraft flying through a rolled-up wake, aiming to quantify the loads resulting from its interaction with the wake of a leader aircraft or rotorcraft. This is done by measuring the wake-induced forces and moments experienced by the rotor when crossing the wake vortices on an oblique trajectory at a small angle and at the altitude of their centers. Three airspeeds of the follower rotorcraft are investigated: 100, 50, and 25 kt. In these simulations, the encountered wake is that produced by the same rotorcraft flying at 100 kt.

4.1 Numerical setup

The numerical solver, rotor configuration, and trim are identical to those presented in Sections 2 and 3. The wake of the leader rotorcraft flying at 100 kt is represented by a pair of rolled-up vortices obtained from the wake characterization (cf. Section 3), which are continuously fed into the computational domain.

The wake encounter is simulated along an imposed trajectory, as the objective is to measure the forces and moments experienced by the follower, not its dynamic response. The follower rotorcraft is initially located at a lateral distance of $4D$ relative to the center of the two-vortex system. In an initial phase, it flies parallel to the wake vortices to properly establish its own wake. Once this wake is well developed, the rotorcraft changes direction to follow an oblique trajectory with a lateral speed component of 5 kt relative to the two-vortex system. Through simulations performed for two lateral velocities (2 kt and 5 kt), it was verified that, as long as this component remains small compared to the TAS, its magnitude has a limited impact on the magnitude of forces and moments experienced by the rotor (with a difference in maximum pitching moment of about 7%). The resulting loads are therefore close to those that would be measured at any position along the trajectory if the rotor were held fixed at that location.

While accelerating laterally to reach the target lateral speed (at a rate of 25 $m\ s^{-2}$), the rotor also accelerates in yaw to align itself with the new oblique velocity vector, the magnitude of which equals the TAS and remains constant. This is done by adequately decreasing the streamwise component of the rotor velocity. Thus, the trim remains valid throughout the maneuver. Once the terminal lateral speed is reached, the helicopter maintains its velocity until the end of the simulation. The trim is also maintained; hence, the forces and moments measured when crossing the wake are solely due to the influence of that wake on the rotor.

The spatial resolution is 64 points per rotor diameter. Based on a grid-convergence study, the chosen spatial resolution was found to be sufficient to capture the wake encounter phenomena considered in this work. The computational domain extends $2D$ upstream of the rotor center. At 100 kt, it extends $10D$ downstream; at 50 and 25 kt, it extends $6D$ downstream. The lateral and vertical dimensions of the computational domain dynamically adapt to the positions of the rotorcraft and of its wake. No atmospheric turbulence is added for the wake crossing simulations.

4.2 Wake-induced aerodynamic loads

Volume renderings of the vorticity magnitude, illustrating the rotorcraft shortly after wake crossing, are presented in Figure 9 for the 50 kt and 25 kt cases. Figure 10 displays the wake-induced perturbations in yawing, pitching, and rolling moments, as well as in lift force, as functions of the lateral distance of the rotor relative to the vortex pair. This configuration corresponds to a port encounter, i.e., a scenario in which the port side of the rotor first encounters the starboard wake vortex.

The principal wake-induced loads are a yawing moment, a pitching moment, and a lift force. The yaw and lift perturbations vary symmetrically with respect to the center of the wake, whereas the pitching moment exhibits an essentially antisymmetric behavior.

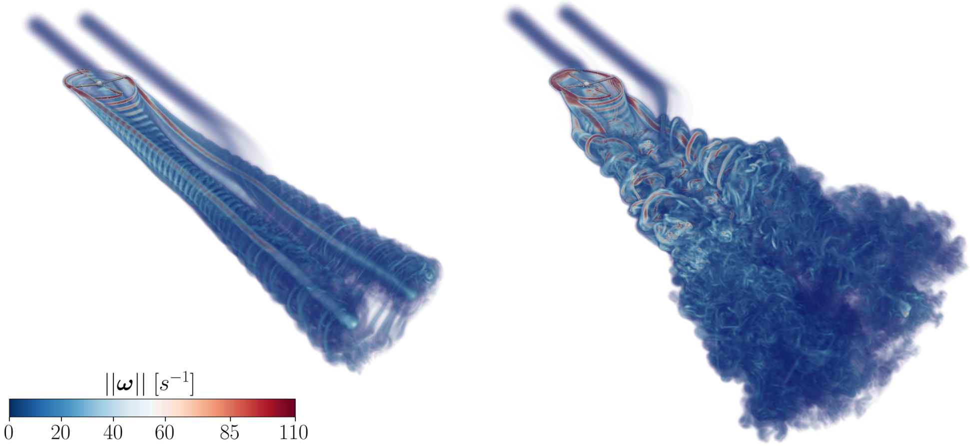

Fig. 9 Volume rendering of $\|\omega\|$ for the cases of wake crossing at 50 kt (left) and 25 kt (right)

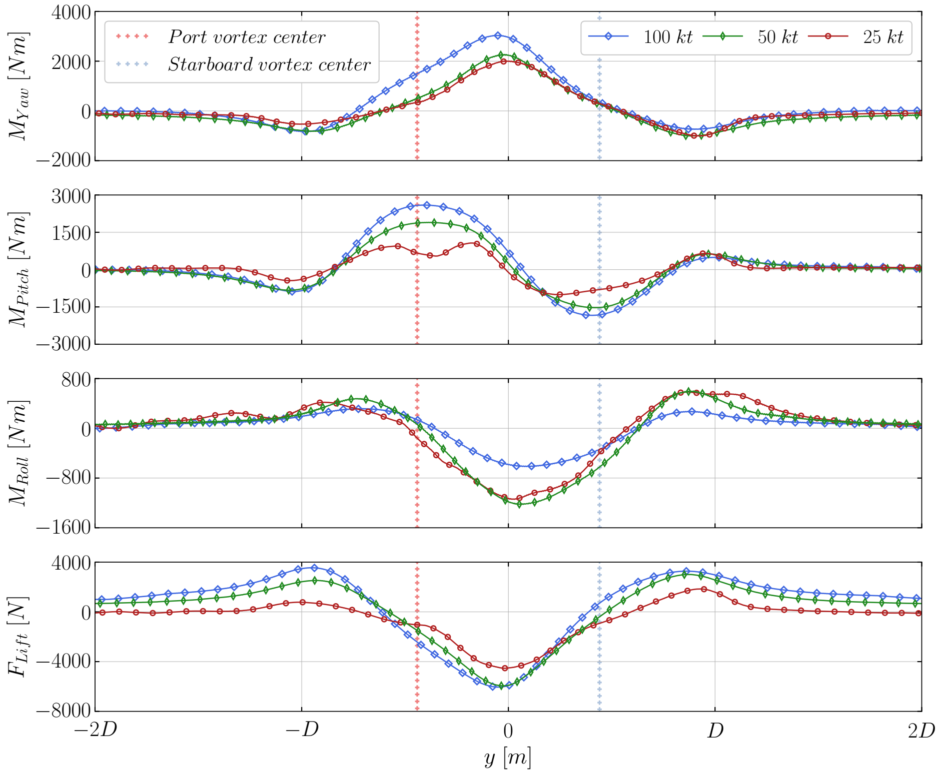

Fig. 10 Aerodynamic moments and lift upsets resulting from the wake encounter at 100, 50, and 25 kt

While a fixed-wing aircraft primarily experiences a rolling moment and lift disturbances when crossing a pair of counter-rotating vortices, a rotorcraft is predominantly affected by a pitching moment [25]. This behavior reflects the fundamental 90° phase shift characteristic of flapping rotors (see [45]).

The pitching moment M_{Pitch} exhibits a similar profile at 100 and 50 kt, with peak values occurring near the vortex centers. At 25 kt, the pitching moment becomes less smooth, as the rotorcraft is more sensitive to fluctuations in its own wake at this low airspeed.

Notably, numerical results reveal a monotonic relationship between the maximum value of M_{Pitch} and the flight speed U_∞. This is rather counter-intuitive, as the wake-induced velocity field is not dependent on the flight speed of the follower. Consequently, the velocity field experienced by the blades is not a simple superposition of wake-induced and rotor-induced components. This strongly suggests a non-linear coupling between the wake-induced velocity field and blade aerodynamics, arising from the combination of several phenomena: the azimuthal asymmetry of disk loading (between the advancing and retreating sides of the rotor), the wake-induced modification of blade angle of attack, and blade flapping, a feature suspected to play a central role in this non-linear behavior.

In addition, the pitching moment response exhibits a noticeable asymmetry between encounters with the port and starboard wake vortices, with larger extrema associated with the port vortex. It can be interpreted as the result of a non-linear combination of rotor azimuthal asymmetry and wake-induced inflow: when encountering the port vortex, the wake-induced velocity reinforces the advancing/retreating-side asymmetry of blade angle of attack, whereas for the starboard vortex both effects partially compensate each other. The persistence of this asymmetry, despite rotor trim, further supports the presence of a strongly non-linear coupling involving blade aerodynamics, blade flapping, and wake deformation.

4.3 Equivalent lateral cyclic angle

As proposed in [31], the pitching moment due to the velocity field induced by a wake vortex is equivalent to that produced by a certain value of the lateral cyclic angle θ_{1s}. This equivalent lateral cyclic angle can thus serve as a useful metric for characterizing a wake encounter.

The maximum pitching moment experienced by a rotorcraft during a wake encounter occurs when flying through the vortex center. The vortex-induced velocity $v_{vort}(r)$ causes a local variation in blade angle of attack, $\alpha_{vort}(r) = v_{vort}(r)/(\Omega\, r)$, which alters blade loading and induces a pitching moment. To quantify the impact of the wake on rotorcraft dynamics, a theoretical equivalent lateral cyclic pitch angle $\theta_{1s,eq}$ is defined, such that the associated induced velocity is $v_{cyc}(r) = (\Omega\, r)\, \theta_{1s,eq}$. This corresponds to the virtual cyclic control input required to generate a pitching moment equal to that induced by a vortex-centered encounter. It is obtained by equating the pitching moment induced by the wake with that produced by this virtual lateral cyclic angle:

$$\int_0^R \frac{1}{2}\rho\,(\Omega\,r)^2\,c(r)\,C_{l,\alpha}\,\alpha_{vort}(r)\,r\,dr = \int_0^R \frac{1}{2}\rho\,(\Omega\,r)^2\,c(r)\,C_{l,\alpha}\,\theta_{1s,eq}\,r\,dr \tag{17}$$

where $C_{l,\alpha}$ is the aerodynamic derivative of the local airfoil, $c(r)$ is the chord distribution, and R is the rotor radius. Further assuming that the blade chord c does not vary with r, this simplifies to:

$$\int_0^R v_{vort}(r)\,r^2\,dr = \int_0^R \left((\Omega\,r)\,\theta_{1s,eq}\right)\,r^2\,dr \tag{18}$$

Thus

$$\theta_{1s,eq} = \frac{4}{\Omega\,R^4}\int_0^R v_{vort}(r)\,r^2\,dr \tag{19}$$

For an encounter with the wake shed by a leader rotorcraft flying at 100 kt, and using the corresponding measured circulation distribution, this simplified model yields $\theta_{1s,eq} = 0.89°$.

It must be emphasized that this highly simplified analysis neglects the forward velocity of the follower rotorcraft, effectively assuming hover conditions. Its applicability to forward flight can only be assumed, and must be verified. This verification is the object of the following analysis.

To assess the validity of the simplified theoretical expression in forward flight, one may compute the actual equivalent cyclic control angle based on the measured pitching moment, denoted $\theta^*_{1s,eq}$. This is achieved by determining the derivative of the pitching moment with respect to the lateral cyclic angle, $M_{Pitch,\theta_{1s}} = \frac{\partial M_{Pitch}}{\partial \theta_{1s}}$. The derivative is obtained by measuring M_{Pitch} for several values of θ_{1s} under steady conditions, followed by a linear regression of the resulting data. The equivalent lateral cycling angle is then computed as follows:

$$\theta^*_{1s,eq} = \frac{M_{Pitch}}{M_{Pitch,\theta_{1s}}} \tag{20}$$

The equivalent lateral cyclic angle is presented in Figure 11 for the three TAS values of interest, and are also compared to the theoretical equivalent cyclic angle $\theta_{1s,eq}$, which does not account for flight speed. The extrema of the equivalent lateral cyclic angle for the three TAS of interest are listed in Table 4.

The simplified metric predicts a constant equivalent angle of 0.89°, independent of the airspeed of the follower. At 100 kt and 50 kt, this simplified estimate underpredicts the actual maximum equivalent angle, whereas at 25 kt, it overpredicts it. Although the simplified model provides values of the correct order of magnitude, the discrepancies remain significant. These differences arise from the port-starboard anti-symmetry of the local relative velocity field experienced by the blades in forward flight, combined with the simplified linear nature of Eq. (17). As a result, flight speed U_∞ cannot be accounted for within such a simplified framework.

Table 4 Extrema of the computed equivalent lateral cyclic angle

$\mathbf{U}_\infty$	[kt]	**100**	**50**	**25**
min $(\theta^*_{1s,eq})$	[deg]	- 1.40	- 1.12	- 0.55
max $(\theta^*_{1s,eq})$	[deg]	1.13	0.85	0.57

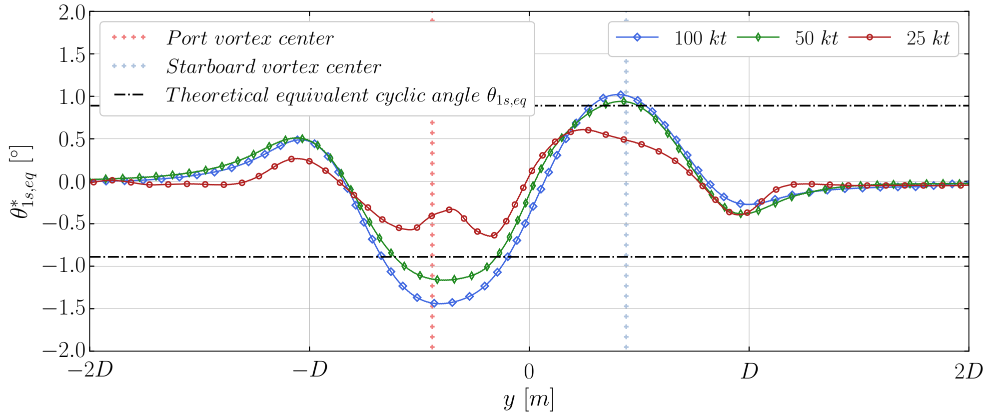

Fig. 11 Computed equivalent lateral cyclic angle as a function of the rotorcraft lateral position at 100, 50, and 25 kt

5 Conclusions

In this study, Large Eddy Simulations of a helicopter rotor in forward flight were performed using the a Vortex Particle-Mesh method with Immersed Lifting Lines, coupled with a multi-body rigid dynamics integrator. Two research questions were addressed. First, how does the rotorcraft's airspeed influence its wake properties, and what is the resulting hazard to a follower aircraft? Second, how does the airspeed of a follower rotorcraft affect the perturbations it experiences when flying through a wake? The key findings of this study are summarized below:

Rotorcraft wake characterization

- For the first time, a systematic characterization of the far wake of a rotorcraft flying from high to very low airspeeds was achieved using a numerical method capable of accurately capturing the wake transport, turbulence and deformation phenomena.
- At low airspeeds (25 and 12.5 kt TAS), the wake departs from classical fixed-wing and high-speed rotorcraft behavior. The wake decay is rapid and coherent vortical structures are only visible in the vicinity of the rotor. The inverse proportionality between vortex circulation and TAS breaks down due to increased vortex spacing, turbulent diffusion, and loss of symmetry around each vortex center.
- The diffused nature of the wake vortices at low airspeeds translates into much larger vortex cores. Consequently, the radial profiles of circulation and induced velocity are significantly different from those of fixed-wing aircraft and rotorcraft at high airspeeds.
- The potential hazard to a following fixed-wing aircraft, measured using the rolling moment coefficient (RMC) metric, is inversely proportional to the TAS at high airspeeds, but saturates at low airspeeds. It also decreases rapidly downstream at low airspeeds.

Rotorcraft flying through a wake

- The simulations presented here constitute the first effort to capture the wake-rotor interactions across a range of follower airspeeds (100-25 kt) while accounting for the two-way coupling between wake vortices and rotor aerodynamics, thus waiving the need for the "frozen vortex" assumption.
- At low follower airspeeds, non-linear coupling between the wake-induced velocity field and rotor blade dynamics leads to significant deformation of the vortices near the rotor. The pitching moment scales with the follower TAS in a nontrivial way. To explain the observed non-linear coupling and its dependence on airspeed, future work should employ high-fidelity simulations resolving the fine blade-vortex interaction phenomena, and also including the elastic blade deformation.
- The encounter severity metric proposed by Padfield et al. [31] was evaluated by comparing its estimate with the pitch perturbation measured in simulations. Owing to its simplified character, the metric fails to capture the speed dependence observed in the numerical results, though it provides a useful first-order approximation of encounter severity.

This work provides valuable insights into low-speed wake phenomena of rotorcraft operating out of ground effect, as well as into the perturbations experienced by a rotor when flying through a wake. By doing so, it contributes to a foundation for future developments of separation matrices that explicitly account for rotorcraft as both leaders and followers. Future studies could investigate rotorcraft wakes at low speeds in ground effect and also include a representation of the fuselage and tail rotor to capture the early development stages of the wake more accurately. Further research on wake encounters experienced by rotorcraft should also include full dynamic and pilot-in-the-loop simulations, while preserving adequate fidelity in modeling the rotor-wake coupling. In addition, extending the present analysis to other rotorcraft architectures involving multiple rotors and/or tilt-rotors would be of interest to assess the impact of rotor configuration on wake structure and encounter severity.

References

[1] Poinsot, T., Corjon, A.: Vortex model to define safe aircraft separation distances. J. Aircr. **33**(3), 547–553 (1996) https://doi.org/10.2514/3.46979

[2] Zhou, J., Chen, Y., Li, D., Zhang, Z., Pan, W.: Numerical simulation of aircraft wake vortex evolution and wake encounters based on adaptive mesh method. Eng. Appl. Comput. Fluid Mech. **14**(1), 1445–1457 (2020) https://doi.org/10.1080/19942060.2020.1835736

[3] Graham, F., Rooseleer, F., Treve, V., De Visscher, I.: Wake turbulence recategorisation on approach and departure for safe and more efficient air traffic management. 30th Congress of the International Council of the Aeronautical Sciences (2016)

[4] Wilson, P., Lepadatu, C., Barnes, S., Lang, S.: Aircraft accident report 1/93. Civil Aviation Authority (1993)

[5] Wilson, P., Lepadatu, C., Barnes, S., Lang, S.: Technical report to support the safety case for recategorization of ICAO wake turbulence standards: An overview of key aviation accidents sometimes assumed to have been caused by wake turbulence. EUROCONTROL and FAA TR-RECAT-2010e (2010)

[6] Authority, C.A.: CAP 493: Manual of Air Traffic Services—Part 1 (2012)

[7] Connor, A.B., O'Bryan, T.C.: A brief evaluation of helicopter wake as a potential operational hazard to aircraft (1962)

[8] Teager, S.A., Biehl, K.J., Garodz, L.J., Tymczyszym, J.J., Burnham, D.C., et al.: Flight test investigation of rotorcraft wake vortices in forward flight. Technical report, Federal Aviation Administration Technical Center (US) (1996)

[9] Köpp, F.: Wake-vortex characteristics of military-type aircraft measured at airport Oberpfaffenhofen using the DLR laser doppler anemometer. Aerospace Science and Technology **3**(4), 191–199 (1999) https://doi.org/10.1016/S1270-9638(99)80042-X

[10] Jimenez-Garcia, A., Barakos, G., Treve, V., Rooseleer, F., Cappellazzo, V., Graham, R.: Helicopter wake encounters in the context of RECAT-EU (2017)

[11] Line, A.J., Brown, R.E.: Efficient high-resolution wake modeling using the vorticity transport equation. AIAA J. **43**(7), 1434–1443 (2005) https://doi.org/10.2514/1.13679

[12] He, C., Zhao, J.: Modeling rotor wake dynamics with viscous vortex particle method. AIAA J. **47**(4), 902–915 (2009) https://doi.org/10.2514/1.36466

[13] Mccroskey, W.: Vortex wakes of rotorcraft. In: 33rd Aerospace Sciences Meeting and Exhibit, p. 530 (1995). https://doi.org/10.2514/6.1995-530

[14] Komerath, N., Smith, M.J.: Rotorcraft wake modeling: past, present and future (2009)

[15] Wang, Y., White, M., Barakos, G., Tormey, P., Pantazopoulou, P.: Simulation of a light aircraft encountering a helicopter wake. Journal of Aircraft **52**(2), 510–523 (2015) https://doi.org/10.2514/1.C032761

[16] Caprace, D.-G., Chatelain, P., Winckelmans, G.: Wakes of rotorcraft in advancing flight: A large-eddy simulation study. Phys. Fluids **32**(8) (2020) https://doi.org/10.1063/5.0015162

[17] Caprace, D.-G., Ning, A.: Large eddy simulation for empirical modeling of the wake of three urban air mobility vehicles. J. Am. Helicopter Soc. **68**(4), 42002–42017 (2023)

[18] Caprace, D.-G., Winckelmans, G., Chatelain, P.: Assessment of the vortex particle-mesh method for efficient LES of hovering rotors and their wakes. In: AIAA Scitech 2021 Forum, p. 0738 (2021). https://doi.org/10.2514/6.2021-0738

[19] Dunham Jr, R.E., Holbrook, G.T., Campbell, R., Van Gunst, R., Mantay, W.: Flight-test experience of a helicopter encountering an airplane trailing vortex. In: Annual National Forum of the American Helicopter Society (1976)

[20] Mantay, W.R., Holbrook, G.T., Campbell, R.L., Tomaine, R.L.: Flight investigation of the response of a helicopter to the trailing vortex of a fixed-wing aircraft. In: Atmospheric Flight Mechanics Conference (1976)

[21] Mantay, W.R., Holbrook, G.T., Campbell, R.L., Tomaine, R.L.: Helicopter response to an airplane's trailing vortex. Journal of Aircraft **14**(4), 357–363 (1977) https://doi.org/10.2514/3.58784

[22] Dreier, M.E.: The influence of a trailing tip vortex on a thrusting rotor. PhD thesis, Pennsylvania State University (1977)

[23] Saito, S., Azuma, A., Kawachi, K., Okuno, Y.: Study of the dynamic response of helicopters to a large airplane wake (1986)

[24] Saito, S., Azuma, A., Okuno, Y., Hasegawa, T.: Numerical simulations of dynamic response of fixed and rotary wing (1987)

[25] Kim, K.-C., Bir, G., Chopra, I.: Helicopter response to an airplane's vortex wake (1986)

[26] Curtiss, H., Zhou, Z.-g.: The dynamic response of helicopters to fixed wing aircraft wake encounters. In: Theoretical Basis of Helicopter Technology Conference, Nanjing Aeronautical Institute, Nanjing, People's Republic of China (1985)

[27] Whitehouse, G., Brown, R.: Modelling a helicopter rotor's response to wake encounters. The Aeronautical Journal **108**(1079), 15–26 (2004) https://doi.org/10.1017/S0001924000004954

[28] Padfield, G.D., Manimala, B., Turner, G.P.: A severity analysis for rotorcraft encounters with vortex wakes. In: Presented at the 28th European Rotorcraft Forum, vol. 25, p. 1 (2002)

[29] Turner, G.P., Padfield, G.D., Harris, M.: Encounters with aircraft vortex wakes: the impact on helicopter handling qualities. Journal of aircraft **39**(5), 839–849 (2002) https://doi.org/10.2514/2.3004

[30] Whitehouse, G., Brown, R.: Modeling the mutual distortions of interacting helicopter and aircraft wakes. Journal of Aircraft **40**(3), 440–449 (2003) https://doi.org/10.2514/2.3139

[31] Padfield, G.D., Lawrence, B., Taghizad, A.: Rotorcraft wake vortex encounters: A flight mechanics perspective. 32nd European Rotorcraft Forum Proceedings, Maastricht (2006)

[32] Lawrence, B., Padfield, G.D.: Wake vortex encounter severity for rotorcraft in final approach. Aerospace science and technology **12**(5), 385–397 (2008) https://doi.org/10.1016/j.ast.2007.09.006

[33] Chatelain, P., Curioni, A., Bergdorf, M., Rossinelli, D., Andreoni, W., Koumoutsakos, P.: Billion vortex particle direct numerical simulations of aircraft wakes. Comput. Methods Appl. Mech. Eng. **197**(13-16), 1296–1304 (2008) https://doi.org/10.1016/j.cma.2007.11.016

[34] Sbalzarini, I.F., Walther, J.H., Bergdorf, M., Hieber, S.E., Kotsalis, E.M., Koumoutsakos, P.: PPM–a highly efficient parallel particle mesh library for the simulation of continuum systems. J. Comput. Phys. **215**, 566–588 (2006) https://doi.org/10.1016/j.jcp.2005.11.017

[35] Cocle, R., Winckelmans, G., Daeninck, G.: Combining the vortex-in-cell and parallel fast multipole methods for efficient domain decomposition simulations. J. Comput. Phys. **227**, 9091–9120 (2008) https://doi.org/10.1016/j.jcp.2007.10.010

[36] Winckelmans, G.S.: Vortex Methods. Encyclopedia of Computational Mechanics, John Wiley and Sons (2004)

[37] Caprace, D.-G., Chatelain, P., Winckelmans, G.: Lifting line with various mollifications: theory and application to an elliptical wing. AIAA J. **57**(1), 17–28 (2019)

https://doi.org/10.2514/1.J057487

[38] Caprace, D.-G., Chatelain, P., Winckelmans, G.: An immersed lifting and dragging line model for the vortex particle-mesh method. Theor. Comput. Fluid Dyn. **34**(1-2), 21–48 (2020) https://doi.org/10.1007/s00162-019-00510-1

[39] Dyachuk, E., Goude, A., Bernhoff, H.: Dynamic stall modeling for the conditions of vertical axis wind turbines. AIAA J. **52**(1), 72–81 (2013) https://doi.org/10.2514/1.J052633

[40] Mann, J.: Wind field simulation. Probabilistic Eng. Mech. **13**(4), 269–282 (1998) https://doi.org/10.1016/S0266-8920(97)00036-2

[41] De Visscher, I.: Interaction of wake vortices with the atmosphere and the ground: Advanced numerical simulation and operational modeling. PhD thesis, Université catholique de Louvain (2012)

[42] Docquier, N., Poncelet, A., Fisette, P.: Robotran: a powerful symbolic generator of multibody models. Mech. Sci. **4**(1), 199–219 (2013) https://doi.org/10.5194/ms-4-199-2013

[43] Kampa, K., Enenkl, B., Polz, G., Roth, G.: Aeromechanic aspects in the design of the EC135. J. Am. Helicopter Soc. **44**(2), 83–93 (1999) https://doi.org/10.4050/JAHS.44.83

[44] Caprace, D.-G.: Modeling of lifting-dragging devices for large eddy simulation of space developing wakes : application to wings, rotors and formation flight. PhD thesis, Université catholique de Louvain (2020)

[45] Padfield, G.D.: Helicopter flight dynamics: the theory and application of flying qualities and simulation modeling. John Wiley and Sons (2008)